Geophysical Research Letters

RESEARCH LETTER
10.1029/2023GL102991

Special Section:
Hydrogeodesy: Understanding changes in water resources using space geodetic observations

Key Points:
- Interferometric Synthetic Aperture Radar (InSAR) revealed the progressive surface uplift and subsequent recovery in West Texas induced by wastewater disposal
- The Bayesian Monte Carlo approach suggests an excess of subsurface volume in the well near the deformation center
- InSAR spatio-temporal data improve estimates for local hydro-geomechanical properties

Supporting Information:
Supporting Information may be found in the online version of this article.

Correspondence to:
W. Zheng,
weiyuz@smu.edu

Citation:
Zheng, W., Lu, Z., Denlinger, R. P., & Kim, J.-W. (2023). Bayesian Monte Carlo inversion of InSAR time series deformation induced by wastewater injection: A case study in West Texas. *Geophysical Research Letters*, *50*, e2023GL102991. https://doi.org/10.1029/2023GL102991

Received 26 JAN 2023
Accepted 9 MAY 2023

Bayesian Monte Carlo Inversion of InSAR Time Series Deformation Induced by Wastewater Injection: A Case Study in West Texas

Weiyu Zheng[1], Zhong Lu[1], Roger P. Denlinger[2], and Jin-Woo Kim[1]

[1]Roy M. Huffington Department of Earth Sciences, Southern Methodist University, Dallas, TX, USA, [2]US Geological Survey, Vancouver, WA, USA

Abstract Wastewater disposal can induce detectable surface uplift, which may cause ground instability and threaten infrastructure. The distributions of local hydro-geomechanical parameters, especially Young's modulus and hydraulic conductivity, play an essential role in these geohazards. To constrain these parameters, we have inverted spatio-temporal deformation measured by Interferometric Synthetic Aperture Radar (InSAR) and injection information using a Bayesian Monte Carlo approach with a poroelastic finite element model. Sentinel-1A/B imagery from 2014 to 2020 is processed to track the spatio-temporal deformation in Winkler county, West Texas, USA. The posterior distribution of subsurface effective volumes reveals under-reported volumes in the well near the deformation center. In addition, the inversion results provide better constraints for the parameters than those solely obtained based on the cumulative spatial deformation or temporal development of the deformation center.

Plain Language Summary Wastewater disposal into injection wells is the most common way to manage the produced water in the oil and gas industry. It can cause surface uplift and influence ground stability. The surface deformation is mainly controlled by the local properties of the rocks and injection volumes. We measured the time-series deformation in West Texas using satellite radar images and then inverted for the properties of rocks with numerical methods. In addition to estimating the local properties of rocks, our results show under-reported volumes at the dominant well.

1. Introduction

West Texas, one of the most prolific hydrocarbon-producing regions in the world, has recently been explored by energy companies because of the rich undiscovered resources (Gaswirth et al., 2018) as well as the application of improved oil recovery (IOR) and enhanced oil recovery (EOR) methods (Zapivalov, 2015). To manage the produced water in the oil and gas industry, the most common way is to inject wastewater into porous rock formations through disposal wells. Improper management of wastewater not only causes environmental and health concerns (Johnston et al., 2016) but also induces detectable surface uplift (Loesch & Sagan, 2018), which may further cause ground instability and threaten the infrastructures. The coupling of the pore fluid pressure to the rock deformation is usually considered a poroelastic process. Pressurized fluid injection forces fluid into the subsurface reservoir, thereby increasing pore fluid pressure in the reservoir that propagates outward from the well with time. This pressure perturbation causes deformation in the overlying strata and induces geodetically-detectable surface deformation and even seismicity (Tung et al., 2021). The local hydro-geomechanical parameters, especially Young's modulus and hydraulic conductivity, play an essential role in this poroelastic process because they control the pore pressure distribution and hence surface uplift (Newell et al., 2017). Reliable estimates are therefore critical to risk prediction and minimization. However, precise local hydro-geomechanical parameters are seldom obtainable due to the lack of well logs in West Texas.

Interferometric Synthetic Aperture Radar (InSAR) is an effective tool to map ground deformation. With centimeter-to-millimeter level precision and meter-level resolution in a large region, this method has proven the capacity to detect surface deformation uplift induced by fluid injection on a localized or regional scale (Kim & Lu, 2018; Samsonov et al., 2015; Staniewicz et al., 2020). Previous studies indicated that InSAR observation can provide constraints on mechanical parameters (Yang et al., 2015) and hydrogeologic parameters (Shirzaei et al., 2019). The parameters of interest can be solved by jointly inverting the deformation observed by InSAR and well injection information (e.g., injection volume and depth, fluid density and temperature) (Shirzaei

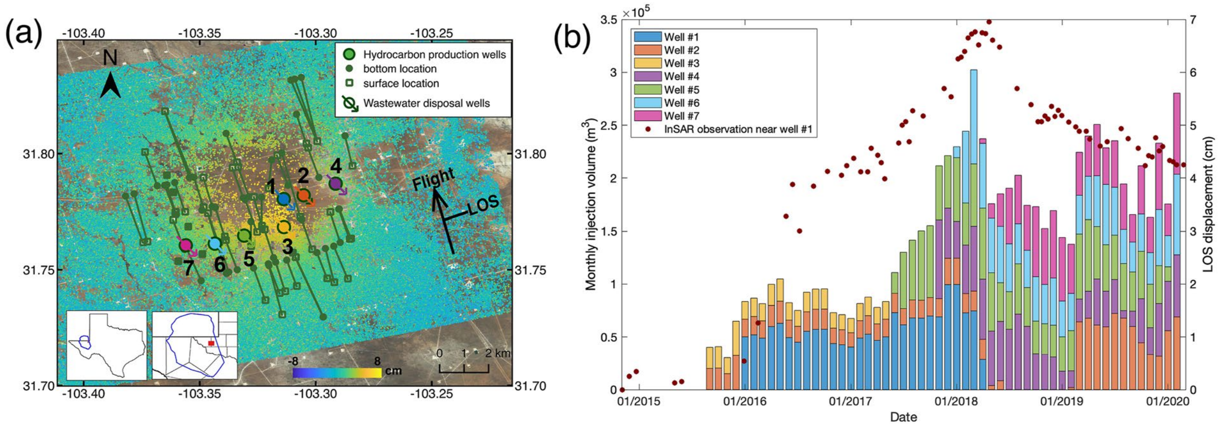

Figure 1. Background information in the research area. (a) Maximum cumulated line-of-sight (LOS) deformation map from November 2014 to May 2018. Color-coded circles with arrows and green symbols indicate the location of 7 wastewater disposal wells and 55 hydrocarbon production wells active during the research period in the deformation area, respectively. Horizontal wells are plotted as green lines linking the surface and bottom locations. The blue contour in the lower left panels represents the boundary of the Delaware basin and the red rectangle marks the research area. (b) Reported monthly injection volumes of the 7 wastewater disposal wells (color-coded bars) from the Railroad Commission of Texas (Texas RRC) and time series of InSAR LOS deformation near well #1 (red circles).

et al., 2019). The spatial time-series deformation derived by InSAR can provide a powerful constraint on the poroelastic process, but due to stringent computational constraints, many studies used only one spatial map (e.g., the cumulative deformation (Shirzaei et al., 2019), an interferogram (Alghamdi et al., 2020)) or temporal deformation at one location (Deng et al., 2020).

The finite element method (FEM) is widely used to solve poroelastic problems related to fluid injection, because it allows material heterogeneity, irregular boundaries, distributed mechanical loads, and multiple fluid sources (Denlinger & O'Connell, 2020; Kim & Deo, 2000; Yin et al., 2011). FEM is based on the Galerkin weighted residual procedure and a finite element discretization of the physical domain. Defmod (Ali, 2014) is a finite element code based on Biot's poroelastic theory (Biot, 1941) that has been successfully used to model deformation induced by wastewater disposal (Zheng et al., 2019) as well as to investigate deformation in a geothermal field (Ali et al., 2018). We estimate parameters using the results from these numerical simulations based on the Bayes theorem (Bishop, 2006).

The Bayesian inversion (Idier, 2013) has been applied to various geophysical inverse problems (Shen et al., 2013) including many poroelastic applications for the characterization of poroelastic materials using various data, such as InSAR measurements (Bagnardi & Hooper, 2018) and acoustical and mechanical measurements (Chazot et al., 2012). The Bayesian approach can quantify the constraints and prior conditions on model parameters, resulting in maximum a posteriori (MAP) estimates and confidence intervals of each parameter. Thus we can constrain our model parameters using both InSAR and well measurements, and include a priori knowledge of the parameters as well as data and model errors. The Monte Carlo method (Sambridge & Mosegaard, 2002) is a robust optimization method and has been widely implemented to characterize a posterior probability distribution in the Bayesian inference.

We use InSAR to measure the surface uplift induced by wastewater disposal at a site in West Texas. Deng et al. (2020) observed the uplift and modeled the surface deformation at the well with the maximum injection volume using a five-layer model assuming poroelastic behavior. In this research, The InSAR-derived spatio-temporal deformation is simulated by poroelastic FEM. A Bayesian Monte Carlo approach is applied to solve for local Young's modulus, hydraulic conductivity, and subsurface effective volumes, which can help understand the underlying mechanism and shed insights into the local hydrogeology.

2. Methods

2.1. Research Area

The study site is located in the Delaware Basin, a hydrocarbon-rich sedimentary basin in West Texas (Figure 1a). The geologic stratigraphy is shown in Table S1 in Supporting Information S1 according to previous geologic research (Beauheim & Holt, 1990; Dutton et al., 2003; Freeze & Cherry, 1979; Mercer, 1983; Nance, 2009; Richey et al., 1985) and well logs from Enverus™. We divide the strata into three layers for the simulation based on the rock composition of each formation. The injection zone is determined by referring to the injection depths of the wastewater disposal wells (Table S1 in Supporting Information S1). It comprises Bell Canyon and Cherry Canyon because of their relatively-high hydraulic conductivities, in which the wastewater can diffuse away rapidly. Above the injection zone, the caprock is defined to be the layers above the Delaware Mountain Group, formed in upper and post Permian. Although the Rustler Aquifer and the post-Permian sediments are pervious, formations from Lamar to Yates with impervious rock composition can be regarded as confining layers, allowing the simplification of one-layer caprock. Underneath the injection zone, the Brushy Canyon and the Bone Spring formation are considered to be base rock with relatively low hydraulic conductivities, preventing the diffusion of the wastewater.

Seven injection wells and fifty-five production wells were active in the research period (Figure 1, Table S2 in Supporting Information S1). Only the injection wells near the deformation center contribute to the surface deformation (Deng et al., 2020). Thirteen production wells are located in the Bone Spring formation (~2.8 km deep), and the other forty-two wells produce from the Wolfcamp formation (~3.5 km deep). Monthly injection volume records of the wastewater disposal wells (Figure 1b) are archived in the Railroad Commission of Texas (Texas RRC).

2.2. InSAR Processing

SAR images from November 2014 to February 2020 acquired from ascending track P78 of Sentinel 1A/B are processed to measure the surface deformation. The C-band data (wavelength of 5.55 cm) are sensitive to detect small magnitude deformation and the short time interval (6 or 12 days) allows temporally dense observations. To obtain the spatiotemporal deformation, the Stanford Method for Persistent Scatterers (StaMPS) (Hooper, 2008), a software that incorporates persistent scatterer and small baseline methods and is widely used for estimating time-series deformation precisely (more details in Hooper et al., 2004, 2007 and Hooper, 2008), is applied to extract coherent pixels, mitigate atmospheric artifacts (primarily in water-vapor rich summer), and track surface movements at the persistent scatterers. Because the InSAR observations are relative in space and time, the first acquisition date (November 2014) and clusters of pixels distant from the deforming location assuming that the neighboring area is not experiencing significant deformation are used for references in both domains. The time-series line-of-sight (LOS) deformation maps are downsampled using quadtree downsampling (Dutton et al., 2003) for model simulation to reduce computation and maintain enough significant information on the deformation pattern.

2.3. Forward Poroelastic Finite Element Model

To simulate InSAR observed deformation, a three-layer three-dimensional finite element model is built. 107,654 tetrahedral elements are generated in the mesh file to describe the geometry of the three-layer geologic settings and the injection points. The elements are denser near the injection points for better spatial resolution (Figure S2 in Supporting Information S1). The mesh covers an area of 20 km × 20 km, and the origin point of the mesh is set to the surface location of the dominant well #1. The vertical direction of the top surface is set to be a free surface while other boundaries are set far away and fixed because the horizontal displacement in the far field is negligible. We suppose the geologic settings in the research area are laterally homogenous because the InSAR observation seems to be spatially continuous without abrupt jumps (Figure S1a in Supporting Information S1), and the research site is localized (~2 km radius). We analyze fluid injection using the poroelastic module of Defmod (Ali, 2014) and solve for the surface deformation resulting from the fluid injection. The fundamental equations (Lewis & Schrefler, 1998; Zienkiewicz & Taylor, 2000) based on Biot's theory consist of momentum conservation (Equation 1) and the continuity equation for mass conservation (Equation 2):

$$\nabla \cdot \sigma - \alpha \nabla p = \boldsymbol{f}, \ \ \sigma = \mathbf{D}\epsilon, \tag{1}$$

where $\mathbf{D}$ is the elasticity matrix which can be represented with Young's modulus E and Poisson's ratio ν, $\boldsymbol{\alpha}$ is the tensor matrix for Biot's coefficient,

$$C\dot{p} - \nabla \cdot \frac{K}{\rho_f g} \nabla p - \boldsymbol{\alpha\epsilon} = q, \tag{2}$$

where $C = \frac{\alpha-\varphi}{K_s} + \frac{\varphi}{K_f}$, φ is porosity, K_s is the bulk modulus of rock, K_f is the bulk modulus of fluid, K is hydraulic conductivity, ρ_f is the fluid density.

The coupled system of equations can be rewritten as Equation 3 using the finite element method:

$$\begin{aligned} \boldsymbol{K}_e\boldsymbol{u} - \boldsymbol{H}\boldsymbol{p} &= \boldsymbol{f} \\ \boldsymbol{H}^T\dot{\boldsymbol{u}} + \boldsymbol{S}\dot{\boldsymbol{p}} + \boldsymbol{Q}\boldsymbol{p} &= \boldsymbol{q} \end{aligned} \tag{3}$$

where $\boldsymbol{K}_e$ is solid stiffness matrix, $\boldsymbol{H}$ is the coupling matrix, $\boldsymbol{S}$ is the compressibility matrix, $\boldsymbol{Q}$ is the fluid permeability matrix, $\boldsymbol{u}$ is the displacement field, $\boldsymbol{f}$ is the body force, $\boldsymbol{p}$ is the pressure vector and $\boldsymbol{q}$ is the volumetric flow into and out of the well. The mesh file, along with information including material properties, boundary conditions, time steps, and injection volumes are plugged into Defmod to solve the governing equations.

Reported injection/production records are collected mainly from Texas RRC, the primary state regulator of oil-related activities in Texas, and Enverus™. Due to the monthly reported volume, the time step is set to one month. The output is the three-dimensional displacement field. We then convert both vertical and horizontal displacements to the LOS direction, and interpolate the time-series deformation to dates of InSAR observed data for further comparison.

2.4. Bayesian Monte Carlo Approach

In a Bayesian framework, the posterior probability density function (PDF), $p(\mathbf{m}|\mathbf{d})$, can be computed from the prior PDF $p(\mathbf{m})$ that modulates any prior information about the model parameters $\mathbf{m}$ independent of the observed data, and the likelihood function $p(\mathbf{d}|\mathbf{m})$ expresses the probability distribution of $\mathbf{d}$ when the parameters are given as $\mathbf{m}$. The un-normalized posterior distribution $p(\mathbf{m}|\mathbf{d})$, based on the misfit between $\mathbf{d}$ and the predicted model, is:

$$p(\mathbf{m}|\mathbf{d}) \propto p(\mathbf{d}|\mathbf{m})p(\mathbf{m}) \tag{4}$$

here the data vector $\mathbf{d} = \{d^1, d^2, \ldots, d^n\}$ are the spatio-temporal deformation observed by InSAR ($n = 66$ is the number of InSAR images), the model parameters $\mathbf{m} = \{m^1, m^2, \ldots, m^l\}$ are Young's modulus, hydraulic conductivities in three layers, and the scaling factors of effective volumes to reported volumes in injection well #1 ($l = 7$ is the number of total model parameters). If the poroelastic model is defined as $\mathbf{G}$, then the likelihood function is simply related to the standard deviation of all the data-model misfits, defined here as $S(\mathbf{G}(\mathbf{m}),\mathbf{d})$, as:

$$p(\mathbf{d}|\mathbf{m}) = \exp(-0.01 \times S(\mathbf{G}(\mathbf{m}), \mathbf{d})) \tag{5}$$

The Markov Chain Monte Carlo samples the model space to generate the evolution of posterior distribution. An initial series of model parameters $\mathbf{m}_{i=0}$ is selected from prior information, where i is the number of iterations. A new series of model parameters can be generated by making a perturbation to each parameter of $\mathbf{m}_i$ and plugged into Defmod to generate a new finite element model and provide a new simulation of time-series ground deformation. The likelihood functions $p(\mathbf{d}|\mathbf{m}_i)$ and $p(\mathbf{d}|\mathbf{m}_{i+1})$ are then recomputed. The Metropolis law defines the probability of acceptance for model parameters $\mathbf{m}_{i+1}$:

$$P_{\text{accept}} = \begin{cases} 1 & \text{if } p(\mathbf{d}|\mathbf{m}_{i+1}) \geq p(\mathbf{d}|\mathbf{m}_i) \\ p(\mathbf{d}|\mathbf{m}_{i+1})/p(\mathbf{d}|\mathbf{m}_i) & \text{if } p(\mathbf{d}|\mathbf{m}_{i+1}) < p(\mathbf{d}|\mathbf{m}_i) \end{cases} \tag{6}$$

We define the threshold of acceptance $\chi_{\text{crit}} = \chi_{min} + 0.25$, where χ_{min} is the minimum misfit (Figure S3 in Supporting Information S1). Here we choose the initial values by referring to previous research (Zheng et al., 2019).

3. Results

3.1. InSAR Analysis

We observe surface uplift and the follow-on recovery over an area with a radius of ∼2 km at the site in Winkler and Loving counties, West Texas (Figure 1a). Compared to the smaller amount of average monthly production volumes from deeper formations, the larger volumes and shallower depths of injection are more likely to

10.1029/2023GL102991

contribute to surface uplift that we have measured with InSAR. The maximum deformation of ∼7 cm is observed near the injection well #1 around May 2018 (Figure 1a), exactly at the end of the injection of this well. The deformation began to recover afterward, and the approximately flat pattern after May 2018 indicates a mild disposal scheme in terms of ground instability. In addition, the start of the uplift coincided with the start of injection in well #1, and the trend of the InSAR time series matches with the monthly injection record of well #1 (Figure 2a). Taking both the spatial proximity and temporal agreement into account, well #1 can be considered the dominant well for the observed deformation, thus we have added the scaling factor of injection volume in well #1 into model parameters (discussed in Section 4.1).

With results from Bayesian inversion of the InSAR spatio-temporal observations, the best-fit simulation is calculated from the forward poroelastic finite element modeling plugging in the MAP estimates of model parameters including Young's modulus, hydraulic conductivity, and the scaling factor of injection volume in well #1. Uncertainty is calculated based on the standard deviation of accepted models from the Monte Carlo method. Spatial maps of InSAR displacements and the best-fit simulation based on the Bayesian Monte-Carlo approach in May 2018 (i.e., the maximum displacement) (Figure 2b) and the end of the research period (Figure 2c) are compatible with each other. The simulation of the temporal evolution of the maximum displacement point (near well #1) agrees closely with the observation, especially the change in the displacement rate after March 2019.

3.2. Estimated Injection Volumes and Hydro-Geomechanical Parameters

Marginal posterior probability distributions are plotted in Figure 2d, where the MAP probability estimates, the confidence intervals of the model parameters, and the joint distributions between pairs of parameters can be found.

The estimated effective injection volumes are found to be ∼2.6 times as much as the reported volumes in the dominant well #1. This disparity is qualitatively reasonable. Based on the assumption of no heterogeneity and no abrupt temporal change of the hydro-mechanical parameters, if there is no excess of reported volumes in well #1, similar uplift would be expected in March 2019 because of the comparable reported volumes from well #2 (Figure 1b). However, no uplift has been observed by our InSAR analysis (discussed in Section 4.1). As no other injection is found in this area, this discrepancy leads to the skepticism of reported injection volumes from the oil company. The results of effective volumes could provide invaluable information for wastewater disposal management and regulation.

Young's modulus in the caprock, the injection zone, or the base rock approaches 80 GPa, which is comparatively high but still within the reasonable range in West Texas (Yang et al., 2015). Young's modulus can be well constrained in all three layers no matter whether the layer is a confining layer or not.

As for hydraulic conductivity, the situation is different. The best-fit simulation suggests the hydraulic conductivity in the injection zone to be 5.97×10^{-8} m/s, seemingly a bit low when compared to the frequently used values of Bell Canyon 10^{-6}–10^{-7} m/s (Deng et al., 2020) but still within the reasonable range (Beauheim & Holt, 1990). The reason can be the fact that the injection zone could involve not only sandstone but also siltstone or dolostone. The disparity of only half of a magnitude is acceptable considering the combination with Cherry Canyon. This result confirms the feasibility of the division of the injection zone layer. Unlike Young's modulus, hydraulic conductivity in caprock and base rock fails to be constrained. This should be attributed to the prior distribution based on the fact that the caprock and the base rock are confining layers (Table S1 in Supporting Information S1). When those two layers are set to be impervious, all hydraulic conductivities in the impervious range can seal and preserve fluid in the injection zone. The unconstrained hydraulic conductivities from posterior distributions further suggest the caprock and the base rock can be considered as a single layer each.

Although the hydro-mechanical parameters suffer from site-limited validity because of the complicated local hydrogeology, they can still provide a reference for adjacent oil fields and also help investigate the future evolution of this case.

4. Discussion

4.1. Why Are Injection Volumes Added to Model Parameters?

The InSAR observation data can be separated into three periods: (a) November 2014 to May 2018; (b) May 2018 to February 2019; and (c) March 2019 to February 2020. In period 1, injection in well #1 dominates the uplift

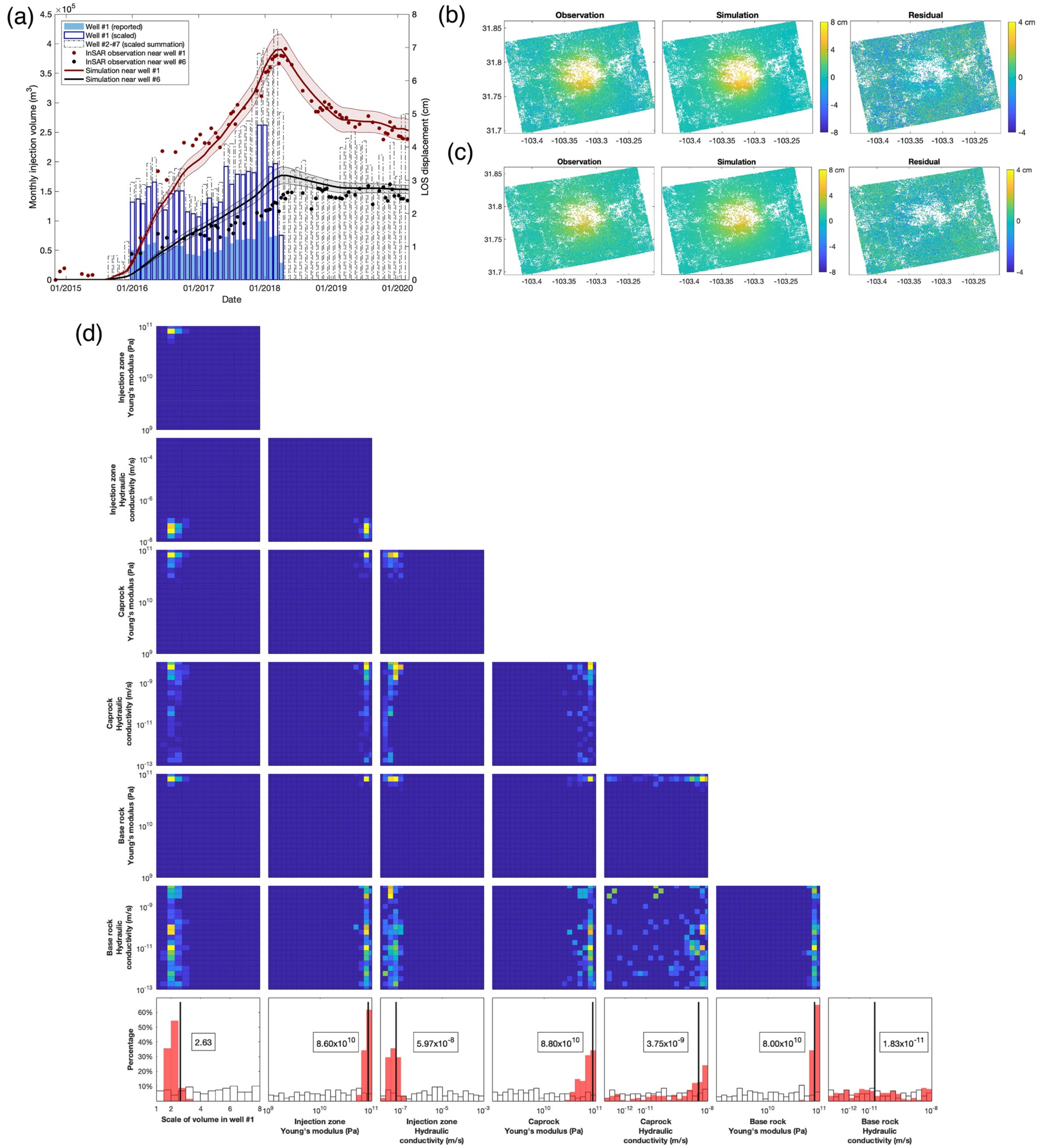

Figure 2. Results from the Bayesian Monte Carlo approach. (a) Comparison between time series displacement from InSAR observation (circles) and the best-fit simulation (solid lines) in the inversion period. Uncertainty is plotted with semi-opaque ranges. Blue-filled and void bars represent the reported volume from RRC and scaled effective volume from the best-fit simulation of well #1, respectively. (b) Maximum cumulative InSAR observed displacement, best-fit simulation, and the residual maps in May 2018. (c) Cumulative InSAR observed displacement, best-fit simulation, and the residual maps at the end of the whole research period with scaled volume. (d) Marginal posterior probability distributions. One-dimensional figures are prior (open histograms) and posterior distributions (red histograms) of all model parameters. Two-dimensional marginals are plotted according to frequency (cold colors for low frequency, warm colors for high frequency).

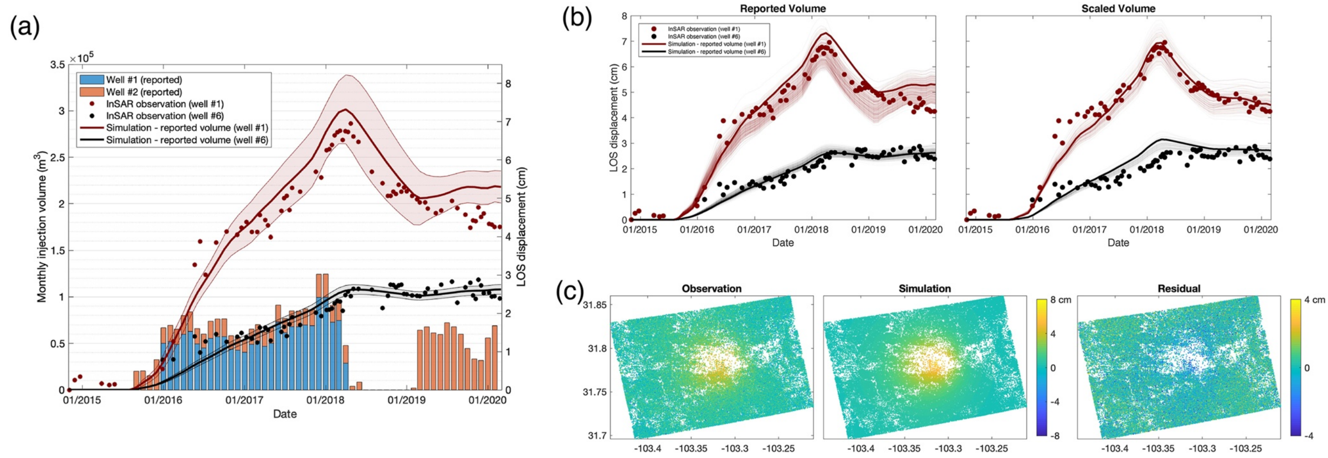

Figure 3. Best-fit results based on fixed reported volume. (a) Comparison between time series displacement from InSAR observation (circles) and the best-fit simulation (solid lines) in the whole research period using reported injection volume from Texas RRC. Uncertainty is plotted with semi-opaque ranges. Reported monthly injection volumes in well #1 and #2 in the whole research period are plotted using bars. (b) Accepted models in one run (30,000 times) are plotted as semi-opaque lines. (c) Maximum cumulative InSAR observed displacement, simulation based on reported injection volume, and the residual map in May 2018.

which occurs at the beginning of this injection and ends at the completion of the injection. In period 2, the uplift starts to recover and keeps at a relatively large deformation rate. As the trend starts directly from the completion of well #1, the whole period 2 can be considered as recovery due to the end of the injection. In period 3, the deformation rate becomes smaller, reflecting some perturbation at around March 2019. Since well #1 has not been reactivated after August 2019 while well #2, which is only 0.5 km from the deformation center, has been reactivated at the start of period 3, the variation of the deformation rate is highly likely due to the reactivation of well #2.

This study was initially proposed to solve local hydrogeology. Thus, the original model parameter set consists of only three Young's modulus and three hydraulic conductivities and the injection volume of well #1 is fixed as the reported volume. The results with reported volumes are plotted in Figure 3. Although we can find some parameters within the reasonable range to fit the observed deformation in periods 1 and 2, we always see a deformation rebounding after the reactivation of well #2 in period 3. The rebound is found not only from the best-fit simulation but all the accepted models (Figure 3b), which means the Bayesian Monte Carlo method cannot return to an acceptable simulation in this time interval if only hydro-geomechanical parameters are used as model parameters.

When the best solution cannot fit surface deformation, both the geologic stratigraphy and injection information could be questioned as they are the two preset components in the inversion. As described in Section 3.2, the unconstrained hydraulic conductivities from posterior distributions in the caprock and base rock can further convince the feasibility of one-layer caprock and base rock each. The depths of geologic layers are implied from well logs which are believed to be relatively accurate. The sample spaces of hydro-geomechanical parameters are in a fairly large range. Hence, we have determined to maintain the geologic stratigraphy and question the injection information.

The two crucial factors in the injection record impacting surface deformation are depth and volume. Supposing the effective depth is in the caprock or base rock where the hydraulic conductivity is low, the wastewater should diffuse away slowly, and the surface deformation after the completion of injection of well #1 should maintain the level or alleviate tardily. Therefore, the abrupt, and almost simultaneous retrieval of the surface uplift after May 2018 suggests retaining the reported depths. Thus, the reported volumes are questioned and we apply scaling factors of the monthly injection volumes of the well(s). In consideration of the spatial proximity between the well locations and the deformation center and the temporal correlation between InSAR detected deformation and the reported injection volumes, we add the scaling factor for injection volume in well #1 into the model parameters to calculate the effective injection volume.

The fact of no rebounding from InSAR itself can provide a piece of evidence for the excess effective volume of well #1. The simulation of rebounding is due to the compatible reported injection volume rate of well #1 in period 1 and well #2 in period 3 and the small distance between these two wells. To fix this problem, the excess of reported volumes in well #1 is a reasonable explanation for the discrepancy of displacements in periods 1 and 3 because it relatively reduces the contribution for surface uplift from injection volumes from well #2. Actually, in the case of scaled volume, some of the accepted models also show the same pattern of rebounding after the reactivated injection volume in well #2 (Figure 3b). The patterns of deformation near well #1 in period 3 show that: the smaller the excess effective volume is, the severer the rebounding is. In addition, Deng et al. (2020) arbitrarily increase the Skempton ratio to solve for the unexpected large deformation in period 1, which also suggests that normal parameters of Young's modulus and hydraulic conductivity cannot fit the InSAR observation. Here we attribute this anomaly to excess effective injection volume.

4.2. Production

As for hydrocarbon production, the deformation rate is almost zero from November 2014 to December 2015 when there was no injection but production, indicating the production events do not induce surface displacement. Hence, we did not include it in the modeling. Taking account of the production in deeper formation that generally induces surface subsidence, adding production information to the inversion will require even more excess injection volume to reach the InSAR observation, thus the conclusion of excess injection volume will remain the same. We provide a rough estimate of the influence of hydrocarbon production with the average injection rate based on yearly production and peak production from Enverus™ in Figure S4 in Supporting Information S1. Although the total hydrocarbon production per month in Wolfcamp formation is comparable with the injection volume, it is less likely to impact the localized surface deformation because it is a semi-pervious aquifer with a large depth. Here we care about production in the shallower Bone Spring formation, which is significantly impervious than the Wolfcamp formation. Although the monthly volume rate of injection per well is ten times larger than the production for Bone Spring formation, the densely distributed production wells still generate subsidence up to 0.7 cm (Figure S4a in Supporting Information S1), which means the excess effective volume could be even larger.

4.3. Tests of Using Fewer Constraints

In this study, we solve the local hydro-geomechanical parameters with InSAR spatio-temporal data as constraints. However, Bayesian inversion incorporating InSAR spatio-tmporal data requires huge computation resources. Therefore, we conduct two new inversion processes to test the possibility of using fewer constraints: spatial constraints and temporal constraints, respectively. In detail, the spatial constraints are from the cumulative spatial deformation map to May 2018; the temporal constraints are from the temporal displacements of the deformation center and the location near well #6. The comparison of the three constraints are plotted in Figure S5 in Supporting Information S1, and the marginal distributions are shown in Figure S6 in Supporting Information S1.

In this case, spatial constraints cannot simulate the temporal evolution, especially in period 3 (Figure S5a in Supporting Information S1). The temporal constraints perform better to simulate period 3 but underfit the spatial deformation range (Figure S5b in Supporting Information S1). The MAP estimates for hydro-geomechanical parameters of the three methods are all at the same magnitude, while spatial constraints and temporal constraints have a smaller scale factor of injection volume in well #1, which explains their failure to simulate period 3. The narrower distributions and the highest probabilities of MAP estimates of spatio-temporal constraints both indicate that utilizing the whole spatio-temporal InSAR data can be used to discard biased solutions substantially and better constrain the model parameters. Therefore, to reduce the computation burden, spatial constraints and temporal constraints are good choices for quick rough results, but if possible, the use of spatio-temporal InSAR data as constraints is a better option for precise local hydrogeology retrieval.

5. Conclusion

In this study, InSAR has been applied to measure the spatio-temporal localized surface displacement related to fluid injection. The surface uplift and recovery afterward at the site in Winkler county, West Texas, is mainly dominated by the wastewater disposal in well #1. The Bayesian Monte Carlo approach with a forward poroelastic finite element modeling performs well to solve the uplift induced by wastewater injection. The best-fit simulation matches well with the InSAR observation data. The posterior distribution provides reasonable MAP estimates and uncertainties of Young's modulus and hydraulic conductivity. The volumes needed to make the results make sense in dominant well #1 are found to be ∼2.6 times than the reported volumes. Compared to other constraints, the Bayesian Monte Carlo approach with a forward poroelastic finite element modeling of InSAR-derived spatio-temporal data as constraint shows its advantages in solving poroelastic problems related to wastewater disposal. Our analysis provides a new technique to estimate local hydrogeologic properties which can serve as a reference for adjacent oil fields. Furthermore, our study can provide insights for wastewater disposal management and regulation.

Data Availability Statement

Sentinel-1 InSAR images can be downloaded from the Alaska Satellite Facility (https://search.asf.alaska.edu) by searching for the Winkler county. The topographic effects were removed using 1-arcsec digital elevation model (DEM) data from the shuttle radar topography mission (SRTM) (NASA JPL, 2013). StaMPS is available at https://homepages.see.leeds.ac.uk/~earahoo/stamps/. Information about fluid injection, hydrocarbon production, and distribution of the wells was obtained from the Railroad Commission of Texas (https://gis.rrc.texas.gov/GISViewer/) by zooming out to the Winkler county. Defmod is available at https://bitbucket.org/stali/defmod. Processed InSAR time-series deformation and the best-fit model are available at https://doi.org/10.5281/zenodo.7566905.

Acknowledgments
This study was funded by NASA Earth Surface and Interior Program (80NSSC21K1474) and NASA-ISRO SAR (NISAR) Science Team (80NSSC22K1888), and the Shuler-Foscue Endowment at Southern Methodist University.

References

Alghamdi, A., Hesse, M. A., Chen, J., & Ghattas, O. (2020). Bayesian poroelastic aquifer characterization from InSAR surface deformation data. Part I: Maximum a posteriori estimate. *Water Resources Research*, *56*(10), e2020WR027391. https://doi.org/10.1029/2020wr027391

Ali, S. T. (2014). Defmod-parallel multiphysics finite element code for modeling crustal deformation during the earthquake/rifting cycle. *arXiv preprint arXiv:1402.0429*.

Ali, S. T., Reinsch, E. C., Moore, J., Plummer, M., Warren, I., Davatzes, N. C., & Feigl, K. L. (2018). Geodetic measurements and numerical models of transient deformation at Raft River geothermal field Idaho, USA. *Geothermics*, *74*, 106–111. https://doi.org/10.1016/j.geothermics.2018.02.007

Bagnardi, M., & Hooper, A. (2018). Inversion of surface deformation data for rapid estimates of source parameters and uncertainties: A Bayesian approach. *Geochemistry, Geophysics, Geosystems*, *19*(7), 2194–2211. https://doi.org/10.1029/2018gc007585

Beauheim, R. L., & Holt, R. M. (1990). Hydrogeology of the WIPP site. In *Geological and hydrological studies of evaporites in the northern Delaware Basin for the Waste Isolation Pilot plant (WIPP)* (Vol. 14, pp. 131–179). *Field Trip*. Geological Society of America (available from Dallas Geological Society).

Biot, M. A. (1941). General theory of three-dimensional consolidation. *Journal of Applied Physics*, *12*(2), 155–164. https://doi.org/10.1063/1.1712886

Bishop, C. M. (2006). *Pattern recognition and machine learning* (p. 738). Springer.

Chazot, J. D., Zhang, E., & Antoni, J. (2012). Acoustical and mechanical characterization of poroelastic materials using a Bayesian approach. *Journal of the Acoustical Society of America*, *131*(6), 4584–4595. https://doi.org/10.1121/1.3699236

Deng, F., Dixon, T. H., & Xie, S. (2020). Surface deformation and induced seismicity due to fluid injection and oil and gas extraction in western Texas. *Journal of Geophysical Research: Solid Earth*, *125*(5), e2019JB018962. https://doi.org/10.1029/2019jb018962

Denlinger, R. P., & O'Connell, D. R. H. (2020). Evolution of stress and tectonic faulting induced by deep fluid injection, Paradox Basin, Colorado. *Bulletin of the Seismological Society of America*, *110*(5), 2308–2327. https://doi.org/10.1785/0120190328

Dutton, S. P., Flanders, W. A., & Barton, M. D. (2003). Reservoir characterization of a Permian deep-water sandstone, East Ford field, Delaware basin, Texas. *AAPG Bulletin*, *87*(4), 609–627. https://doi.org/10.1306/10100201085

Freeze, R. A., & Cherry, J. A. (1979). *Groundwater*. Prentice-Hall, Inc.

Gaswirth, S. B., French, K. L., Pitman, J. K., Marra, K. R., Mercier, T. J., Leathers-Miller, H. M., et al. (2018). *Assessment of undiscovered continuous oil and gas resources in the Wolfcamp shale and bone spring formation of the Delaware Basin, Permian Basin Province, New Mexico and Texas, 2018 (No. 2018-3073)*. US Geological Survey.

Hooper, A. (2008). A multi-temporal InSAR method incorporating both persistent scatterer and small baseline approaches. *Geophysical Research Letters*, *35*(16), L16302. https://doi.org/10.1029/2008gl034654

Hooper, A., Segall, P., & Zebker, H. (2007). Persistent scatterer interferometric synthetic aperture radar for crustal deformation analysis, with application to Volcán Alcedo, Galaápagos. *Journal of Geophysical Research*, *112*(B7), B07407. https://doi.org/10.1029/2006jb004763

Hooper, A., Zebker, H., Segall, B., & Kampes, B. (2004). A new method for measuring deformation on volcanoes and other natural terrains using InSAR persistent scatterers. *Geophysical Research Letters*, *31*(23), L23611. https://doi.org/10.1029/2004gl021737

Idier, J. (Ed.) (2013). *Bayesian approach to inverse problems*. John Wiley & Sons.

Johnston, J. E., Werder, E., & Sebastian, D. (2016). Wastewater disposal wells, fracking, and environmental injustice in southern Texas. *American Journal of Public Health*, *106*(3), 550–556. https://doi.org/10.2105/ajph.2015.303000

Kim, J. G., & Deo, M. D. (2000). Finite element, discrete-fracture model for multiphase flow in porous media. *AIChE Journal*, *46*(6), 1120–1130. https://doi.org/10.1002/aic.690460604

Kim, J. W., & Lu, Z. (2018). Association between localized geohazards in West Texas and human activities, recognized by Sentinel-1A/B satellite radar imagery. *Scientific Reports*, *8*(1), 1–13. https://doi.org/10.1038/s41598-018-23143-6

Lewis, R. W., & Schrefler, B. A. (1998). *The finite element method in the static and dynamic deformation and consolidation of porous media*. John Wiley & Sons.

Loesch, E., & Sagan, V. (2018). SBAS analysis of induced ground surface deformation from wastewater injection in East Central Oklahoma, USA. *Remote Sensing*, *10*(2), 283. https://doi.org/10.3390/rs10020283

Mercer, J. W. (1983). *Geohydrology of the proposed waste isolation pilot plant site, Los Medanos Area, Southeastern New Mexico*. US Department of the Interior, Geological Survey.

Nance, H. S. (2009). *Middle Permian Basinal siliciclastic deposition in the Delaware Basin: The Delaware Mountain Group (Guadalupian)* (p. 180). Bureau Econ. Geol., The University of Texas at Austin.

NASA JPL. (2013). *NASA Shuttle Radar Topography Mission Global 1 arc second*. NASA LP DAAC. https://doi.org/10.5067/MEaSUREs/SRTM/SRTMGL1.003

Newell, P., Yoon, H., Martinez, M. J., Bishop, J. E., & Bryant, S. L. (2017). Investigation of the influence of geomechanical and hydrogeological properties on surface uplift at In Salah. *Journal of Petroleum Science and Engineering*, *155*, 34–45. https://doi.org/10.1016/j.petrol.2016.11.012

Richey, S. F., Wells, J. G., & Stephens, K. T. (1985). *Geohydrology of the Delaware Basin and vicinity, Texas and New Mexico (No. 84-4077)*. Open-File Services Section.

Sambridge, M., & Mosegaard, K. (2002). Monte Carlo methods in geophysical inverse problems. *Reviews of Geophysics*, *40*(3), 3–1. https://doi.org/10.1029/2000rg000089

Samsonov, S., Czarnogorska, M., & White, D. (2015). Satellite interferometry for high-precision detection of ground deformation at a carbon dioxide storage site. *International Journal of Greenhouse Gas Control*, *42*, 188–199. https://doi.org/10.1016/j.ijggc.2015.07.034

Shen, W., Ritzwoller, M. H., Schulte-Pelkum, V., & Lin, F. C. (2013). Joint inversion of surface wave dispersion and receiver functions: A Bayesian Monte-Carlo approach. *Geophysical Journal International*, *192*(2), 807–836. https://doi.org/10.1093/gji/ggs050

Shirzaei, M., Manga, M., & Zhai, G. (2019). Hydraulic properties of injection formations constrained by surface deformation. *Earth and Planetary Science Letters*, *515*, 125–134. https://doi.org/10.1016/j.epsl.2019.03.025

Staniewicz, S., Chen, J., Lee, H., Olson, J., Savvaidis, A., Reedy, R., et al. (2020). InSAR reveals complex surface deformation patterns over an 80,000 km^2 Oil-Producing Region in the Permian Basin. *Geophysical Research Letters*, *47*(21), e2020GL090151. https://doi.org/10.1029/2020gl090151

Tung, S., Zhai, G., & Shirzaei, M. (2021). Potential link between 2020 Mentone, West Texas M5 earthquake and nearby wastewater injection: Implications for aquifer mechanical properties. *Geophysical Research Letters*, *48*(3), e2020GL090551. https://doi.org/10.1029/2020gl090551

Yang, Q., Zhao, W., Dixon, T. H., Amelung, F., Han, W. S., & Li, P. (2015). InSAR monitoring of ground deformation due to CO_2 injection at an enhanced oil recovery site, West Texas. *International Journal of Greenhouse Gas Control*, *41*, 20–28. https://doi.org/10.1016/j.ijggc.2015.06.016

Yin, S., Dusseault, M. B., & Rothenburg, L. (2011). Coupled THMC modeling of CO_2 injection by finite element methods. *Journal of Petroleum Science and Engineering*, *80*(1), 53–60. https://doi.org/10.1016/j.petrol.2011.10.008

Zapivalov, N. P. (2015). Improved oil recovery vs. enhanced oil recovery. Enhanced oil recovery: Methods, economic benefits and impacts on the environment (pp. 81–94).

Zheng, W., Kim, J. W., Ali, S. T., & Lu, Z. (2019). Wastewater leakage in West Texas revealed by satellite radar imagery and numerical modeling. *Scientific Reports*, *9*(1), 1–11. https://doi.org/10.1038/s41598-019-51138-4

Zienkiewicz, O., & Taylor, R. (2000). *The finite element method: The basis*. Butterworth- Heinemann.